J. Fluid Mech. (2001), *vol.* 429, *pp.* 187–216. Printed in the United Kingdom

Direct simulation of turbulent supersonic boundary layers by an extended temporal approach

By THIERRY MAEDER, NIKOLAUS A. ADAMS AND LEONHARD KLEISER

ETH Zürich, Institute of Fluid Dynamics, ETH Zentrum, CH-8092 Zürich, Switzerland

(Received 7 July 1998 and in revised form 18 August 2000)

The present paper addresses the direct numerical simulation of turbulent zero-pressure-gradient boundary layers on a flat plate at Mach numbers 3, 4.5 and 6 with momentum-thickness Reynolds numbers of about 3000. Simulations are performed with an extended temporal direct numerical simulation (ETDNS) method. Assuming that the slow streamwise variation of the mean boundary layer is governed by parabolized Navier–Stokes equations, the equations solved locally in time with a temporal DNS are modified by a distributed forcing term so that the parabolized Navier–Stokes equations are recovered for the spatial average. The correct mean flow is obtained without *a priori* knowledge, the streamwise mean-flow evolution being approximated from its upstream history. ETDNS reduces the computational effort by up to two orders of magnitude compared to a fully spatial simulation.

We present results for a constant wall temperature T_w chosen to be equal to its laminar adiabatic value, which is about $2.5\,T_\infty$, $4.4\,T_\infty$ and $7\,T_\infty$, respectively, where T_∞ is the free-stream temperature for the three Mach numbers considered. The simulations are initialized with transition-simulation data or with re-scaled turbulent data at different parameters. We find that the ETDNS results closely match experimental mean-flow data. The van Driest transformed velocity profiles follow the incompressible law of the wall with small logarithmic regions.

Of particular interest is the significance of compressibility effects in a Mach number range around the limit of $M_\infty \simeq 5$, up to which Morkovin's hypothesis is believed to be valid. The results show that pressure dilatation and dilatational dissipation correlations are small throughout the considered Mach number range. On the other hand, correlations derived from Morkovin's hypothesis are not necessarily valid, as is shown for the strong Reynolds analogy.

1. Introduction

Turbulence modelling of supersonic flows relies – often tacitly – on assumptions about compressibility effects. In a compressible flow, the evolution of the turbulent kinetic energy (TKE) is tied to the evolution of the mean kinetic energy and of the mean internal energy. Compressibility effects reflect themselves in the significance of exchange mechanisms that prevail at sufficiently large Mach number and do not exist in an incompressible flow. From experimental data it has been concluded by Morkovin (1962) that for supersonic boundary layers at Mach numbers M_∞ lower than about 5, density behaves as a passive scalar or as a fluid property, and the

vorticity production due to baroclinic torque remains small. The consequence is that, if mean-density variations are taken into account and if density fluctuations are small compared to mean density, the turbulence structure in wall-bounded shear layers follows closely that of an incompressible fluid (Bradshaw 1977). This is commonly called 'Morkovin's hypothesis', the validity of which is the reason why van Driest's mean-flow scaling (Bradshaw 1977) is successful, as has been shown experimentally (Fernholz & Finley 1980) and numerically (Huang, Coleman & Bradshaw 1995).

Another issue is whether conclusions derived from Morkovin's hypothesis are valid. One of the most important is the strong Reynolds analogy (SRA) which is often used when incompressible turbulence models are applied for compressible flows. The SRA predicts that velocity and temperature fluctuations are perfectly anticorrelated, the correlation coefficient being $R_{u''T''} = -1$. It can be shown that this is true if the fluctuations of pressure and total temperature are negligible (Lele 1994). The SRA, however, is not satisfied at Mach numbers as low as $M_\infty = 3$, as our simulation data will show (see § 3.3.3). Huang *et al.* (1995) found that the SRA in its strict form is not valid for a turbulent channel flow at $M = 3$. The SRA can be extended (Gaviglio 1987) for a known variation of the mean total temperature $\bar{T}_0$, predicting a smaller magnitude of $R_{u''T''}$. Further extensions by Huang *et al.* (1995) suggest that $R_{u''T''}$ scales with the turbulent Prandtl number and the variation $\partial\bar{T}_0/\partial\bar{T}$. Guarini *et al.* (2000) present a thorough derivation and analysis of the SRA equations. They discuss several classical forms of the SRA and some extensions, and compare them with the results of their $M_\infty = 2.5$ boundary-layer simulation. They observe that the predictions of the SRA equations are much better supported by compressible experimental results than by their simulation data and by incompressible experimental results. Guarini *et al.* (2000) explain the better agreement of compressible experimental results with the SRA by the fact that measured total temperature fluctuations, from which SRA correlations are then derived, are considerably smaller than the true values.

An indicator for the significance of compressibility effects is the turbulent Mach number M_t which relates the square root of the turbulent kinetic energy to the mean speed of sound, see equation (3.3). The magnitude of M_t for the turbulent channel flow of Huang *et al.* (1995) and for our boundary-layer data is, in certain regions, larger than the threshold $M_t = 0.3$ below which compressibility effects are considered to be small. The somewhat paradoxical situation arises that conditions leading to the assumption of negligible compressible turbulent correlations are not strictly satisfied and compressibility indicators are rather large, but nevertheless the magnitude of compressible turbulent correlations is negligible even at Mach numbers as high as $M_\infty = 6$, as we will show in § 3.3. A possible explanation is suggested by Sarkar (1995) who found a dependence of the compressibility effects on the gradient Mach number, which is substantially larger for mixing layers than for boundary layers (at comparable free-stream Mach number). Friedrich & Bertolotti (1997) found that the impermeability condition at the wall strongly reduces the integral lengthscale in the wall-normal direction, which could be responsible for the difference in gradient Mach numbers and would support the findings of Sarkar. Ristorcelli (1997) points out that compressibility effects depend on the inverse of a turbulent Reynolds number, which also could justify their insignificance in wall-bounded flows.

Here and in the following, an overbar denotes a Reynolds-averaged quantity and a tilde a Favre-averaged quantity. A single prime indicates a fluctuation with respect to a Reynolds average, and a double prime a fluctuation with respect to a Favre average. Where applicable, we make use of the spanwise homogeneity and averages are obtained by computing the arithmetic mean over time samples and over all

grid points in the streamwise and spanwise directions. The Favre or mass average of a quantity f is computed as $\tilde{f} = \overline{\rho f}/\bar{\rho}$. Favre averaging not only simplifies the averaged compressible Navier–Stokes equations, but is also the natural way of extracting average primitive variables from averaged conservative variables which are the primary variables for a compressible flow. From the equation of state, the Favre-averaged temperature $\tilde{T}$ then appears naturally as the consistent supplement to the set of primitive variables $\bar{\rho}$, $\tilde{u}_i$ and $\bar{p}$.

2. Numerical simulation method

The basic numerical modelling principle follows the temporal direct numerical simulation (TDNS) approach (Kleiser & Zang 1991) allowing the use of periodic boundary conditions in the streamwise and spanwise directions. A sketch of the integration domain is shown in figure 1 together with the Cartesian coordinate system $\{x_1, x_2, x_3\} \equiv \{x, y, z\}$, denoting the streamwise, spanwise and wall-normal coordinates, respectively.

The assumption of streamwise periodicity leads to a temporal growth of the laminar mean-flow profile if the mean flow is not enforced to be a stationary solution, as has been noted by Wray & Hussaini (1984) in transition simulations using TDNS. This problem carries over to a turbulent flow where a non-stationary mean-flow behaviour is obtained when streamwise mean-flow gradients are omitted. For a compressible flow, the mean streamwise velocity profile develops in time in a non-self-similar way, which inhibits correct statistics. To some extent, the mean-flow growth can be taken into account by imposing a given or quasi-simultaneously computed mean flow through the addition of forcing terms to the basic equations. This procedure, using a two-scale analysis, has first been successfully applied to a turbulent incompressible boundary layer by Spalart (1988). In the present work, we employ the extended TDNS (ETDNS) approach, in which the flow is computed at a series of downstream positions (see figure 1), allowing the mean-flow evolution to be approximated from its upstream history.

The effect of the streamwise mean-flow variation on the turbulent fluctuations can be approximated by adding a forcing term to the Navier–Stokes equations, which are solved locally in a streamwise-periodic domain to obtain the instantaneous flow field at the respective spatial station. The forcing is constructed in such a way that the spatial average of the equations which govern the full flow field locally coincides with the equations governing the mean field. The correct mean flow at a fixed spatial station is then obtained as the stationary limit of the mean solution computed from the Navier–Stokes equations with the proper forcing terms, see equation (2.1). Integral mean-flow quantities such as shape factor and skin-friction coefficient are monitored to assess the stationarity of the flow. When a sufficiently stationary state is reached, the computational box can be marched downstream another spatial step. A detailed analysis and validation of this approach is given in Adams *et al.* (2000).

Note that for a comparable spatial simulation (SDNS), memory requirements would be about one order of magnitude and CPU-time requirements about one to two orders of magnitude higher than for the ETDNS approach. This estimate results from the fact that with the ETDNS, a much shorter domain is required (1 to 5 mean boundary-layer thicknesses δ_0 in x instead of 20 to 100 δ_0 for an SDNS (Rai, Gatski & Erlebacher 1995)), the inflow transient is not an issue (costs at best 10 δ_0 in an SDNS according to Lund, Wu & Squires (1998)) and averaging in the homogeneous streamwise direction is allowed. Also, the ETDNS procedure is self-contained in the

sense that no *a priori* assumptions about the mean flow are required, except for the slow streamwise variation that makes the parabolization possible.

2.1. *Equations*

The equations solved at a fixed spatial station are the compressible Navier–Stokes equations in conservative form, whose non-dimensional representation is written as

$$\frac{\partial \boldsymbol{U}}{\partial t} = \frac{\partial \boldsymbol{F}}{\partial x} + \frac{\partial \boldsymbol{G}}{\partial y} + \frac{\partial \boldsymbol{H}}{\partial z} + \boldsymbol{Z}_0 + \boldsymbol{Z}_1. \tag{2.1}$$

The vector $\boldsymbol{U}$ contains the conservative variables $\{\rho, \rho u, \rho v, \rho w, E\}$. The density ρ is normalized with its free-stream value, the three velocity components u, v, w with the free-stream streamwise velocity. E is the total energy defined as

$$E = \frac{p}{\gamma - 1} + \tfrac{1}{2}\rho\left(u^2 + v^2 + w^2\right), \tag{2.2}$$

where γ is the ratio of specific heats (assumed to be constant, $\gamma = 1.4$) and p is the static pressure normalized with twice the free-stream dynamic pressure. The static temperature T and dynamic viscosity μ are both normalized with their free-stream values. The flux vectors $\boldsymbol{F}$, $\boldsymbol{G}$ and $\boldsymbol{H}$ are given by

$$\boldsymbol{F} = \begin{bmatrix} -\rho u \\ -\rho u^2 - p + \tau_{xx} \\ -\rho uv + \tau_{xy} \\ -\rho uw + \tau_{xz} \\ -u(E+p) - q_x + u\tau_{xx} + v\tau_{xy} + w\tau_{xz} \end{bmatrix}, \tag{2.3}$$

$$\boldsymbol{G} = \begin{bmatrix} -\rho v \\ -\rho uv + \tau_{xy} \\ -\rho v^2 - p + \tau_{yy} \\ -\rho vw + \tau_{yz} \\ -v(E+p) - q_y + u\tau_{xy} + v\tau_{yy} + w\tau_{yz} \end{bmatrix}, \tag{2.4}$$

$$\boldsymbol{H} = \begin{bmatrix} -\rho w \\ -\rho uw + \tau_{xz} \\ -\rho vw + \tau_{yz} \\ -\rho w^2 - p + \tau_{zz} \\ -w(E+p) - q_z + u\tau_{xz} + v\tau_{yz} + w\tau_{zz} \end{bmatrix}, \tag{2.5}$$

The shear-stress tensor obeying Newton's relation and Stokes' hypothesis is given by

$$\tau_{ij} = \frac{\mu}{Re}\left(\frac{\partial u_i}{\partial x_j} + \frac{\partial u_j}{\partial x_i} - \frac{2}{3}\frac{\partial u_k}{\partial x_k}\delta_{ij}\right) \tag{2.6}$$

and the heat-flux vector is

$$q_i = \frac{1}{(\gamma - 1)M_\infty^2 Pr}\frac{\mu}{Re}\frac{\partial T}{\partial x_i} \tag{2.7}$$

for $i, j = 1, 2, 3$, with $(u_1, u_2, u_3) \equiv (u, v, w)$. M_∞ is the free-stream Mach number. The computational Reynolds number Re is based on the density, viscosity and streamwise velocity of the free stream and on the displacement thickness of the laminar boundary layer at the beginning of the transition simulation (see § 2.1.2). The Prandtl number Pr is set to be constant and equal to 0.7. The dynamic viscosity μ is assumed to obey Sutherland's law

$$\mu(T) = T^{3/2} \frac{1+S}{T+S} \tag{2.8}$$

where S is 110.4 K divided by the free-stream static temperature. The perfect-gas equation is used as an additional algebraic relation:

$$\gamma M_\infty^2 p = \rho T. \tag{2.9}$$

The forcing terms $\boldsymbol{Z}_0$ and $\boldsymbol{Z}_1$ are described in § 2.2.

2.1.1. *Boundary conditions*

In the streamwise and spanwise directions periodic boundary conditions are assumed which are implicitly satisfied by using a Fourier pseudospectral formulation. At the wall, the no-slip condition is enforced and temperature is kept constant in time and space. Non-reflecting boundary conditions are implemented at the upper truncation plane $z = z_{max}$, using a characteristic formulation for the hyperbolic terms (Thompson 1987).

2.1.2. *Initial conditions*

For case B, specified below, the final turbulent flow field from a separate transition simulation performed with a conventional TDNS (Adams & Kleiser 1996) is taken as the initial condition. The same flow field, rescaled to satisfy the different boundary conditions, is used for cases A and C.

At the first few spatial stations with the ETDNS method, the information about the mean-flow development from previous marching steps is either missing or still inaccurate (at the very first station, the forcing terms are approximated using a laminar similarity solution for the mean flow). This causes a non-physical spatial transient which must first be overcome, and which makes stationarity of the flow more difficult to obtain at the first few marching stations. However, our experience shows that in this spatial transient phase the solution can be marched downstream after the temporal transient has settled down appreciably, even before a stationary state is reached.

2.2. *Extended temporal approach*

In the ETDNS approach, we do not follow the analysis of Spalart (1988), but make use of the parabolic character of the turbulent mean flow directly. The motivation for the procedure originates from the parabolized stability equations (PSE) approach (Herbert 1997), but taking into account the full nonlinear interactions. Since the mean flow changes on a slow scale in the streamwise direction and turbulent fluctuations vary on a fast scale, the flow field can be split into a slowly varying mean-flow part and a fast varying fluctuation part. The latter can be represented accurately in a streamwise periodic domain with the streamwise extent of a few turbulence integral lengthscales. The mean flow, on the other hand, can be approximated well by parabolized Reynolds-averaged Navier–Stokes equations (PRANS), where the nonlinear interaction between mean flow and turbulent fluctuations is taken into account by a Reynolds-stress term. If the PRANS equations are written in a temporal

transient form by adding a time-derivative $\partial \boldsymbol{U}/\partial t$ to their left-hand sides, the forcing terms $\boldsymbol{Z}_0 + \boldsymbol{Z}_1$ can be determined by the following procedure. The streamwise or wall-parallel plane average of equation (2.1) is taken and the components of $\boldsymbol{Z}_0 + \boldsymbol{Z}_1$ are identified as those terms which are missing in the averaged equations when compared to the PRANS equations for the mean flow. For the formulation of $\boldsymbol{Z}_0$ and $\boldsymbol{Z}_1$ refer to the Appendix; a more comprehensive derivation can be found in Adams *et al.* (2000). Computations showed that the forcing term $\boldsymbol{Z}_0$, which represents the influence of the streamwise mean-flow gradients on the mean flow itself, is at least two orders of magnitude larger than $\boldsymbol{Z}_1$, which describes the interaction between the streamwise mean-flow gradients and the turbulent fluctuations.

2.3. *Numerical discretization*

The numerical discretization of the Navier–Stokes equations follows Adams & Kleiser (1996) and Adams *et al.* (2000). In the periodic streamwise and spanwise directions, a pseudospectral Fourier collocation approach is employed. A compact finite-difference scheme is used in the wall-normal direction, which is of sixth order at the inner points and has third- to fourth-order boundary closures for the first- and second-derivative operators (Lele 1992). For time advancement, an explicit third-order compact-storage Runge–Kutta scheme is used (Williamson 1980). Slow-scale streamwise mean-flow gradients are approximated numerically with a backward differentiation scheme, which is of first order for the three first spatial stations and of second order for the subsequent stations. A sixth-order (fourth-order close to the boundaries) compact filter operation (Lele 1992) is applied in the wall-normal direction at each third to fifth timestep in order to remove spurious modes caused by aliasing errors. The filtering is not required for numerical stability. It has been verified that filtering does not affect the results (Adams *et al.* 2000).

The computational grid is Cartesian and equi-distant in the wall-parallel directions. For the wall-normal direction, a combined algebraic/transcendental mapping function between the evenly spaced computational interval $[0, 1]$ and the physical interval $[0, z_{max}]$ is used, in order to allow for a gridpoint condensation near the wall and around the boundary-layer edge.

3. Simulation results

To investigate compressibility effects in semi-bounded supersonic flows we have performed a series of direct numerical simulations at free-stream Mach numbers $M_\infty = 3$ (case A), $M_\infty = 4.5$ (case B) and $M_\infty = 6$ (case C), a range which contains the Mach number limit of $M_\infty \simeq 5$ above which Morkovin's hypothesis is expected to be no longer valid. The momentum-thickness Reynolds number $Re_\theta = \rho_\infty u_\infty \delta_2/\mu_\infty$ for all three cases is around 3000 and the mean streamwise pressure gradient is zero. Table 1 summarizes the physical simulation parameters. The free-stream Mach number M_∞, the wall temperature T_w and the computational Reynolds number $Re = 10^4$ are fixed parameters of the simulations for all three cases. Re_θ, $Re_{\delta_2} = \rho_\infty u_\infty \delta_2/\mu_w$, the skin friction coefficient C_f, the shape factor H_{12} and the ratio of boundary-layer thickness to reference length δ_0/δ_c are simulation results and cannot be enforced in advance (we use here $\delta_0 = \delta_{0,\,99.5\%}$). Displacement and momentum thicknesses are computed as

$$\delta_1 = \int_0^{\delta_0} \left(1 - \frac{\rho u}{\rho_\infty u_\infty}\right) \mathrm{d}z, \quad \delta_2 = \int_0^{\delta_0} \frac{\rho u}{\rho_\infty u_\infty} \left(1 - \frac{u}{u_\infty}\right) \mathrm{d}z,$$

Case	M_∞	Re_θ	Re_{δ_2}	T_w	$C_f \times 10^3$	H_{12}	δ_0/δ_c	δ_1/δ_c	$u_\tau Re/v_w$	u_τ
A	3	3028	1174	2.50	2.02	5.86	0.865	0.324	78.40	0.0498
B	4.5	3305	795	4.38	1.51	8.91	0.690	0.299	32.44	0.0562
C	6	2945	500	6.98	1.14	17.20	0.652	0.392	15.79	0.0614

TABLE 1. Physical simulation parameters.

Case	L_x	L_x^+	L_y	L_y^+	L_z	L_z^+	$N_x \times N_y \times N_z$	t_s	Samples	Steps
A	$1.48\,\delta_0$	549	$0.84\,\delta_0$	314	$3.16\,\delta_0$	1176	$192 \times 144 \times 180$	57.4	43	4
B	$5.52\,\delta_0$	1217	$1.32\,\delta_0$	292	$2.21\,\delta_0$	487	$432 \times 192 \times 200$	178.6	81	4
C	$2.34\,\delta_0$	312	$1.42\,\delta_0$	189	$2.97\,\delta_0$	395	$240 \times 160 \times 220$	226.4	40	5

TABLE 2. Numerical simulation parameters.

respectively. Following Guarini *et al.* (2000), the reference length δ_c is defined as the lowest z-location at which the van Driest transformed mean velocity $\bar{u}_c(z = \delta_c)$ is equal to the free-stream value u_{c_∞}, see equation (3.1). We interpret their definition as $\bar{u}_c(z = \delta_c) = 0.9999\,u_{c_\infty}$. We also give the inverse wall units $u_\tau Re/v_w$ and the friction velocities $u_\tau = \sqrt{\tau_w/\rho_w}$ for the three cases. Note that all data and graphs are non-dimensionalized with free-stream values (see § 2.1) and reference lengths δ_c of the respective mean boundary layers, unless mentioned otherwise.

Numerical simulation parameters are given in table 2. Reynolds and Favre averages have been obtained by averaging over the homogeneous directions (x and y) and over the samples in the time interval t_s within the stationary state at the last ETDNS marching station. The number of samples within t_s and the number of spatial marching steps of the ETDNS method (see § 2) are also given in table 2. Typically, the size of a spatial step is chosen as a few times (ca. 2–7) the length of the computational domain, which corresponds to 5–10 mean boundary-layer thicknesses. This is on the one hand large enough to avoid an overlap of the computational domains at the different stations, and on the other hand sufficiently short so that the local mean boundary-layer thickness increases by not more than about 6% to 8% to ensure that the marching procedure is reasonably accurate. L_x, L_y and L_z are the extents of the computational domain in the respective coordinate directions (see figure 1) and N_x, N_y and N_z the corresponding numbers of grid points. A limiting factor for the spatial domain size of our simulations was the available computer resources. However, consistency with the ETDNS approach also requires L_x to be small enough for the mean-flow variation along L_x to be sufficiently modest. On the other hand, L_x and L_y have to be large enough for turbulent fluctuations to be sufficiently decorrelated over distances $\frac{1}{2}L_x$ and $\frac{1}{2}L_y$ respectively. For these reasons, the domain sizes of our simulations can be considered as minimum. They nevertheless well exceed the dimensions (in wall units) of the minimum channel simulations of Jimenez & Moin (1991) which were about 300 and 100 wall units in the streamwise and spanwise directions, respectively. Jimenez & Moin (1991) found that for these minimum dimensions, second-order statistics were still in excellent agreement with experimental data below $z^+ = 40$ although two-point correlations over distances of half the domain size were rather large. In the incompressible boundary-layer simulation of Spalart (1988) at $Re_\theta = 1410$, the domain size in the streamwise and spanwise directions was 11 400 and 2850 wall units, with a grid spacing of 40 and 13, respectively. Using a simulation technique

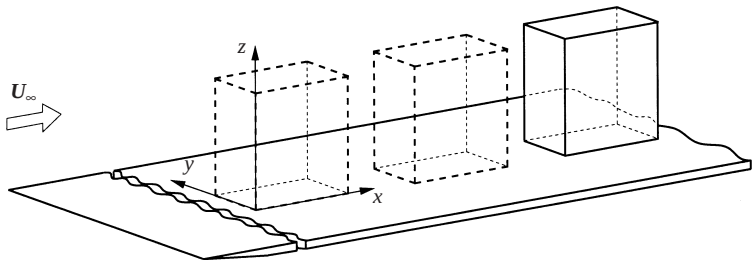

FIGURE 1. Principle of the extended temporal DNS (ETDNS).

similar to Spalart's, adapted for a compressible flow at $M_\infty = 2.5$ and $Re_\theta = 1577$, Guarini *et al.* (2000) found that it was necessary to increase the resolution to give a grid spacing of 9 and 6 wall units in the streamwise and spanwise direction, while reducing the domain sizes to 2269 and 1134 wall units, respectively. Note that a special effort was made in our case B, where the computational domain is longer and the number of statistical samples for the computation of turbulence profiles is larger than for the other cases. We observed, however, that these measures did not change the main trends already found with a smaller domain and fewer samples.

An important parameter affecting the turbulence structure is the type of temperature boundary condition at the wall. For a turbulent flow, a Neumann boundary condition, such as $\partial T/\partial z = 0$, seems inappropriate since a prescribed heat flux would require an instantaneous response of the wall temperature to a temperature fluctuation of the fluid next to the wall. It is more suitable to assume that the wall temperature is constant, since usually the heat capacity of the immersed body is so large that its temperature response is slow compared to the turbulent fluctuations, see also Mack (1984). For the present simulations, we impose the respective laminar adiabatic wall temperature, which can be computed from a similarity solution and is close to the turbulent mean adiabatic wall temperature, since the average heat flux across the wall is small, as our simulation data show (the magnitude of the Stanton numbers is about 10^{-5}). This means that we are considering hot-wall conditions. The effect of the wall temperature on the turbulence structure has been investigated in a separate study (Maeder 2000).

3.1. *Spectra and correlations*

To assess the proper numerical resolution we rely on one-dimensional spectra for the different flow components, as shown in figure 2 for positions z near the end of the buffer layer. We define the spectrum of a flow quantity q (e.g. in the x-direction) as

$$E_{q_x}(k_x, z) := \frac{1}{N_y} \sum_{j=1}^{N_y} \hat{q}(k_x, j, z)\hat{q}(k_x, j, z)^* ,$$

where $\hat{q}(k_x, j, z)$ denotes the one-dimensional Fourier transform of $q(x, y, z)$ (here in the x-direction) and the asterisk the complex conjugate. Averaging is performed in the other wall-parallel direction (here y) and in time, which is not indicated in the above formula for clarity. A drop-off of about 3–4 orders of magnitude in the energy content between the smallest and the largest wavenumber is observed, which is considered to be sufficient.

The two-point correlation functions for the different flow variables are shown in figure 3 at the same wall-normal positions as the spectra. A consequence of the

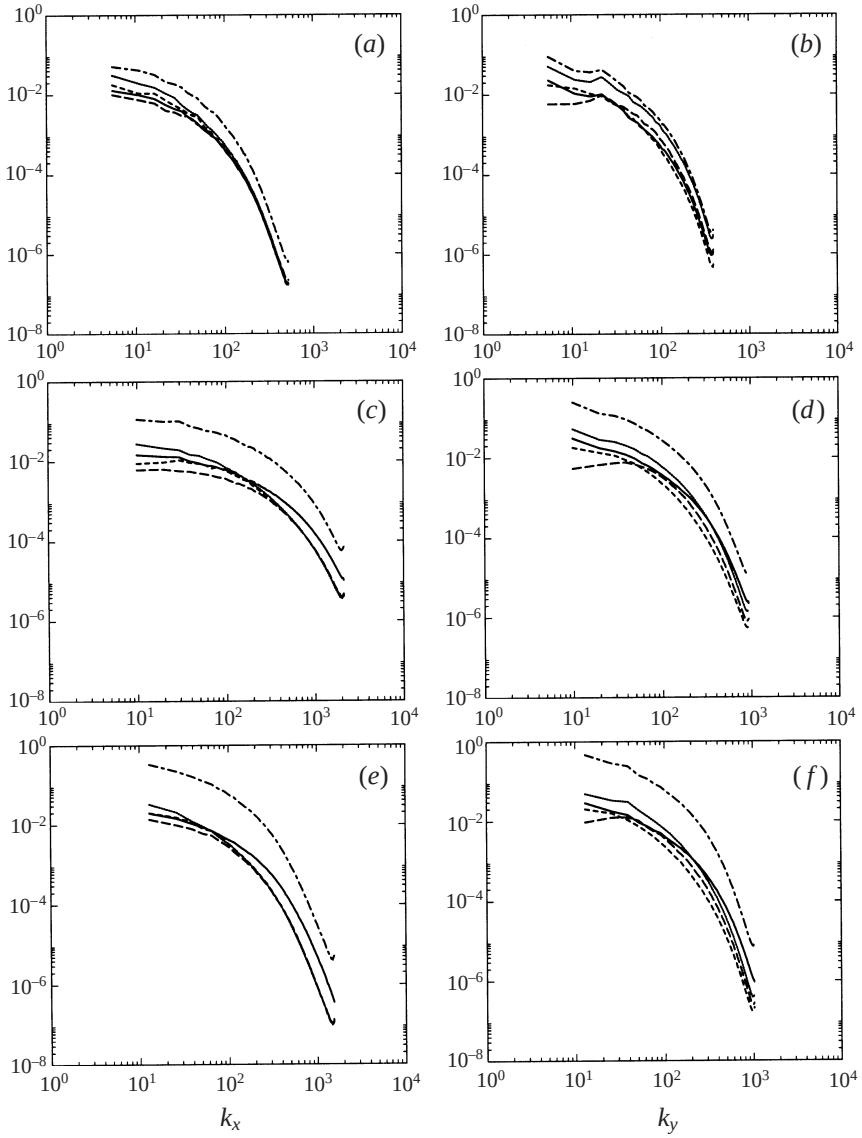

FIGURE 2. One-dimensional spectra; ——, ρ; ···, u; – – –, v; ———, w; —·—, T; (*a*) case A at $z^+ = 21$, x-direction; (*b*) case A at $z^+ = 21$, y-direction; (*c*) case B at $z^+ = 21$, x-direction; (*d*) case B at $z^+ = 21$, y-direction; (*e*) case C at $z^+ = 26$, x-direction; (*f*) case C at $z^+ = 26$, y-direction; wavenumbers scaled by the respective δ_c.

limited extents of the computational domains can be seen in the fact that the two-point correlation functions do not drop to zero at distances $\frac{1}{2}L_x$ and $\frac{1}{2}L_y$, respectively. Case B, with the longest computational domain in wall units, shows slightly improved streamwise two-point correlations compared to cases A and C. For all cases, the two-point correlations of the velocity components v and w decay more rapidly than those of u, ρ and T. Density, temperature and streamwise velocity show a larger coherence across the domain in the streamwise direction, which was also observed for the channel-flow data of Coleman, Kim & Moser (1995) at $M_\infty = 3$.

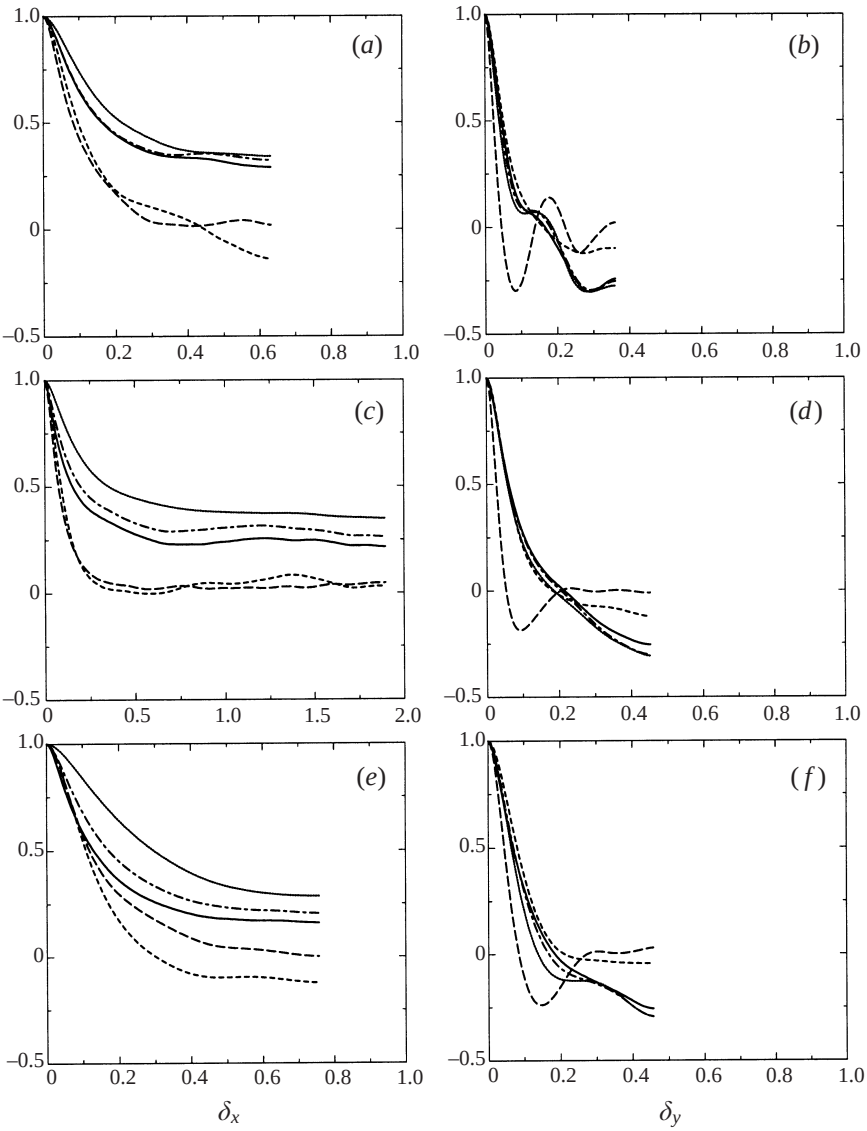

FIGURE 3. Two-point correlation functions; legend as for figure 2.

At Mach numbers that are not too high, density can, for visualization purposes, be considered as a passive scalar. From the density distribution in an (x, z)-plane, we obtain a visualization of the instantaneous flow field for case B which qualitatively corresponds to a streamwise light-sheet exposure of a flow seeded with oil droplets (Smits & Dussauge 1996 p. 225), figure 4(*a*). Turbulent bursting events can be seen where high-density outer fluid sweeps into the boundary layer after low-density near-wall fluid has been ejected into the outer flow. The highly intermittent outer layer is also visible. The position of the boundary-layer edge coincides with a rise of the flatness factor which is observed in the turbulence statistics and indicates increased intermittency, see figure 5.

Near-wall streaks can be visualized by contours of ω_z, the wall-normal vorticity,

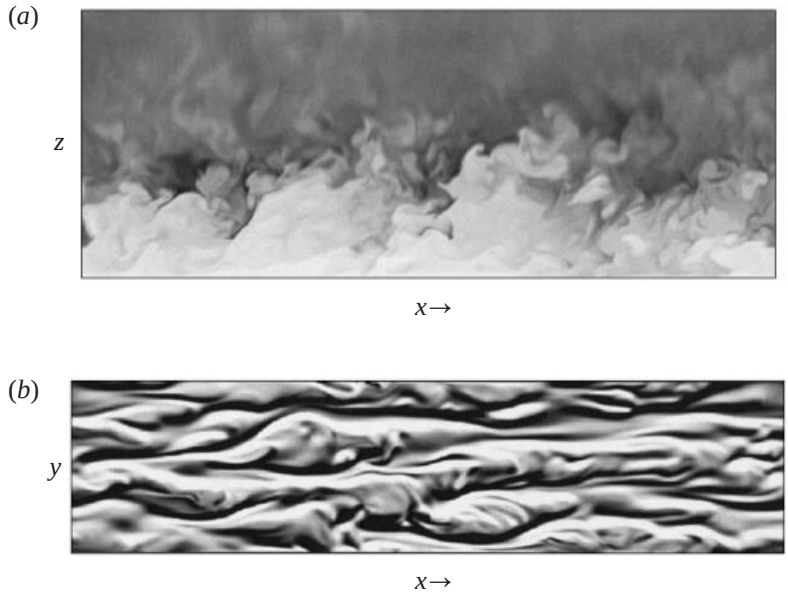

FIGURE 4. (*a*) ρ contours; (*b*) ω_z contours at $z^+ = 10$. Case B, flow from left to right. Extents in the x-, y- and z-directions are 1217, 292 and 487 wall units, respectively.

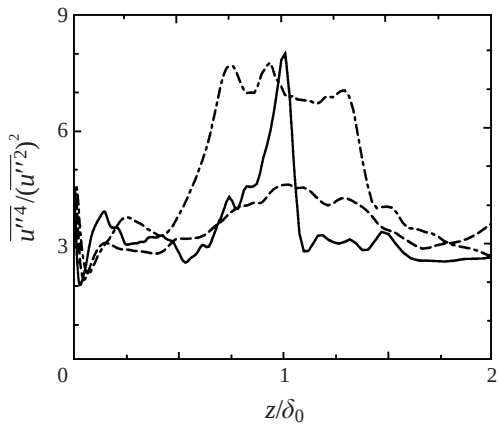

FIGURE 5. Flatness factor $\overline{u''^4}/\left(\overline{u''^2}\right)^2$; ——, case A; – – –, case B; ——–, case C.

shown at $z^+ = 10$ in figure 4(*b*). The spanwise domain size is apparently sufficient to accommodate several near-wall streaks.

3.2. *Mean flow*

Unlike for bounded flows (channels) or unbounded flows (mixing layers), the mean-flow evolution of a temporally evolving boundary layer is considerably different from that of a spatially evolving boundary layer. To be able to compute the mean flow correctly within a temporal simulation, which is a prerequisite for obtaining correct turbulence statistics, we devised the ETDNS approach as explained in § 2. In this section, we compare the mean flow obtained from the ETDNS (without *a priori* assumptions about the mean-flow behaviour) with available experimental data.

Case	M_∞	Re_θ	Re_{δ_2}	T_w/T_∞	$C_f \times 10^3$	H_{12}
7702S0101	3.0	3168	1363	2.67	1.99	5.48
53011001	4.5	3575	880	4.65	1.48	10.01
74021801	4.5	9522	2310	4.77	1.08	9.39
7701S0501	4.5	2486	613	4.69	2.01	7.64
7306S0101	3.9	3403	1035	3.75	1.80	8.83
7306S0102	3.9	3498	1064	3.75	1.76	8.82
7802S0101	2.3	29 254	16 132	2.02	1.44	3.72
7802S0102	2.3	28 797	15 790	2.03	1.45	3.74

TABLE 3. Experimental parameters.

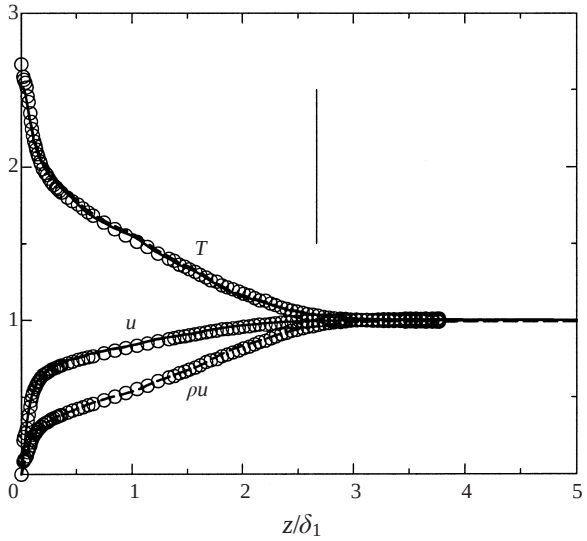

FIGURE 6. Mean-flow profiles of case A compared with experiment (case 7702S0101, symbols); ——, Favre average; – – –, Reynolds average. The vertical line represents the boundary-layer edge.

Mean-flow data which match the Re_θ range of our simulations were found in the data compilations by Fernholz & Finley (1977) and Fernholz & Finley (1981).

The main parameters of the relevant experiments are summarized in table 3, which are identified with an 8- or 9-character string. A comparison of the entries in tables 1 and 3 shows that the experimental and numerical values for the integral parameters $C_f = 2\,(\bar{\mu}/Re)(\overline{\partial u/\partial z})|_w$ and $H_{12} = \delta_1/\delta_2$ agree well. Note that for case B, the data of Coles (53011001) match our Re_θ quite well, while the data of Mabey (74021801) are at a higher Re_θ. The dataset of Mabey (7701S0501) that matches the Reynolds number of case B relatively closely appears to be anomalous as suggested by values of C_f and H_{12} that are inconsistent with both the current simulations and the experimental case of Coles. This dataset will not be considered further. We compare profiles of average velocity $\bar{u}$, $\tilde{u}$, average temperature $\bar{T}$, $\tilde{T}$, and average mass flux $\overline{\rho u}$ with the experimental data. For both cases A and B, we find very good agreement between experiment and ETDNS results, figures 6 and 7. No suitable experimental data were found for case C, the mean-flow profiles of which are shown in figure 8.

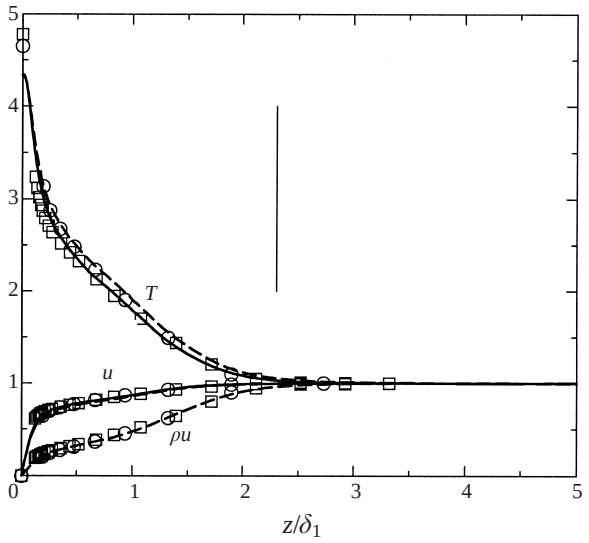

FIGURE 7. Mean-flow profiles of case B compared with experiments, ○, case 53011001; □; case 74021801; ——, Favre average; – – –, Reynolds average. The vertical line represents the boundary-layer edge.

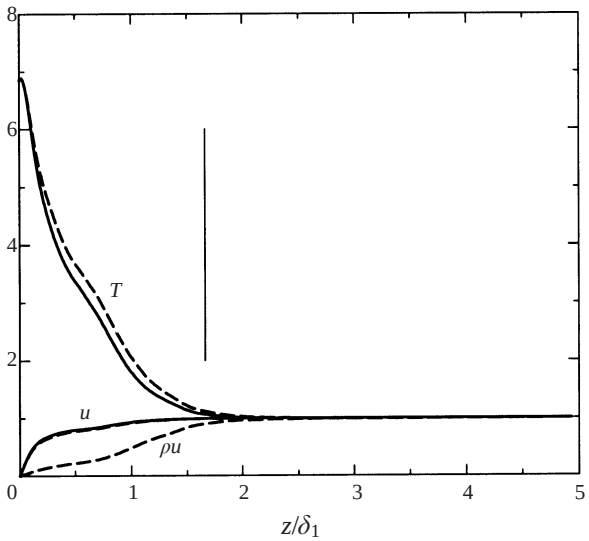

FIGURE 8. Mean-flow profiles of case C; ——, Favre average; – – –, Reynolds average. The vertical line represents the boundary-layer edge.

The deviations between the Reynolds-averaged and Favre-averaged velocity profiles are insignificantly small throughout the considered Mach number range. For the temperature, however, we note an increasing deviation between $\bar{T}$ and $\tilde{T}$ with increasing Mach number. This confirms that density fluctuations become more significant with increasing free-stream Mach number, and that density can no longer be considered as a passive scalar.

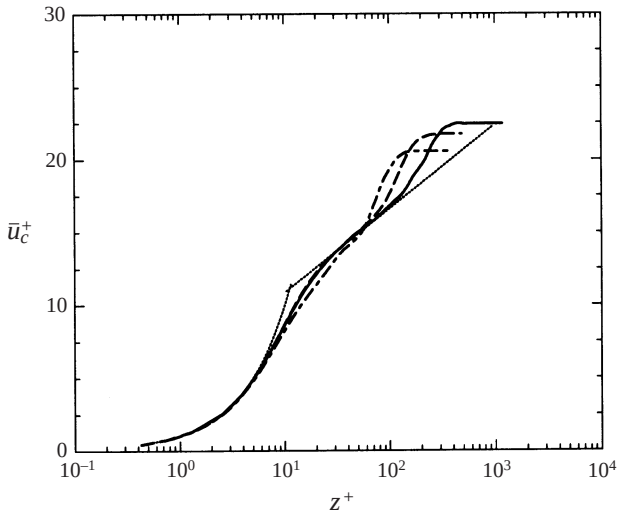

FIGURE 9. Van Driest transformed mean-velocity profiles $\bar{u}_c$ in wall units; ——, case A; – – –, case B; — — —, case C; $\cdots$, law of the wall; $u^+ = z^+$ and $u^+ = (1/0.40)\ln z^+ + 5.1$.

Figure 9 shows the velocity profiles for cases A, B and C after van Driest's transformation (Bradshaw 1977) is applied, which is given by

$$\bar{u}_c^+ = \int_0^{\bar{u}^+} \sqrt{\frac{\bar{\rho}}{\rho_w}}\,\mathrm{d}\bar{u}^+. \tag{3.1}$$

With the van Driest transformation, the profiles collapse better than without transformation. For cases A and B, the data show a logarithmic region $\kappa^{-1}\ln(z^+)+C$, where $\kappa = 0.40$ and $C = 5.1$ as suggested by Fernholz & Finley (1980), more pronounced for the lower free-stream Mach-number case which also has the largest Re_{δ_2}. Owing to the lower Re_{δ_2} in case C, there is no indication of an overlap layer, and the buffer layer connects almost directly to the wake region.

The degree of stationarity of the mean flow is assessed by considering the mean streamwise momentum balance

$$\frac{\partial\overline{\rho u}}{\partial t} = \frac{\partial}{\partial x}\left(-\overline{\rho u^2} - \bar{p} + \overline{\tau_{xx}}\right) + \frac{\partial}{\partial z}\left(-\overline{\rho u w} + \overline{\tau}_{xz}\right) + \left\{\frac{4}{3}\frac{\partial}{\partial x}\left(\frac{\bar{\mu}}{Re}\right)\frac{\partial\bar{u}}{\partial x} + \frac{\partial}{\partial z}\left(\frac{\bar{\mu}}{Re}\frac{\partial\bar{w}}{\partial x}\right)\right\}, \tag{3.2}$$

where the terms in braces are contributed by the forcing term $\boldsymbol{Z}_m$ (see Appendix). The averaged time-derivative of the mean streamwise momentum, computed as the right-hand side of equation (3.2), has been evaluated and normalized with the respective free-stream momentum $\rho_\infty u_\infty$ and large-eddy turn-over time δ_0/u_∞. It can be seen in figure 10 that this quantity remains small throughout the boundary layer, with a maximum magnitude of less than 0.5%.

3.3. *Turbulence structure*

The simulation data of Coleman *et al.* (1995) show that the qualitative differences between the turbulence structure of incompressible and compressible channel flows at $M = 1.5$ and $M = 3$ are very small. The question arises whether a similar behaviour can be observed for boundary-layer flows. A measure for compressibility effects is the

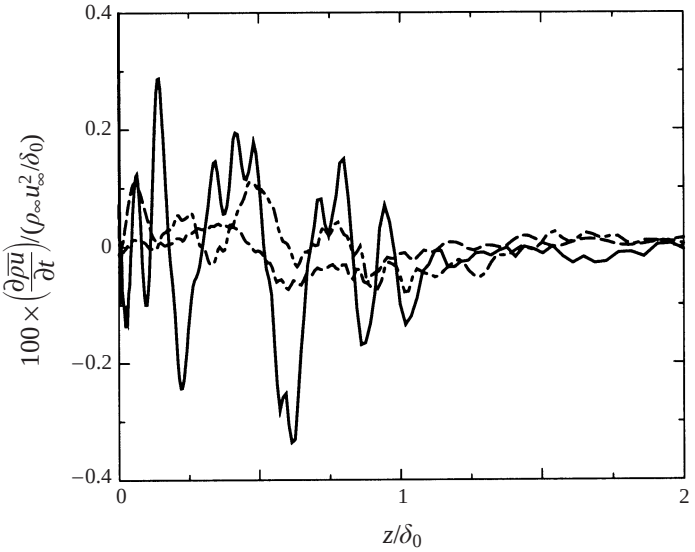

FIGURE 10. Normalized time-derivative of the mean streamwise momentum; ——, case A; – – –, case B; — – —, case C.

turbulent Mach number

$$M_t = \frac{\sqrt{2K}}{\tilde{a}}, \tag{3.3}$$

where $K = \frac{1}{2}\widetilde{u_i''u_i''}$ is the turbulent kinetic energy. The maximum values of M_t, figure 11(*a*), of our three cases are comparable to or larger than those of a mixing layer at a convective Mach number of 0.8 (Luo & Sandham 1995). For case A, M_t is of comparable magnitude to the channel-flow data of Coleman *et al.* (1995). Guarini *et al.* (2000) observe an M_t profile at $M_\infty = 2.5$ with a maximum value of about 0.29, which is similar to our results except that their profile is fuller in the mid-boundary-layer region. The relative density fluctuations r.m.s. $(\rho')/\overline{\rho}$, figure 11(*b*), of case A show a plateau at a value of about 10% from the end of the buffer layer through the logarithmic region into the beginning of the wake region. For case B, we find a rapid increase in the viscous sublayer which becomes weaker in the logarithmic region and a maximum of about 25% in the wake region. Case C exhibits a similar behaviour with a maximum at nearly 40%.

The structure parameter $a_1 = -\overline{u''w''}/(2K)$ remains approximately constant in a range $0.2 \leqslant z/\delta_0 \leqslant 0.7$ where it assumes values between 0.14 and 0.18. For incompressible boundary layers, values between 0.14 and 0.17 have been reported (Smits & Dussauge 1996 p. 215). This could indicate that the turbulence structure in the outer part of supersonic boundary layers is comparable to that of incompressible boundary layers (at least for the present Mach-number range). A similar behaviour was conjectured for late transitional supersonic boundary layers (Adams & Kleiser 1996) from the hypothesis that the relative speed of large-scale structures with respect to the free stream is an indicator of compressibility effects on turbulence structure.

3.3.1. *Reynolds stresses and Reynolds heat fluxes*

The Reynolds normal stresses $\overline{\rho}\,\widetilde{u''u''}$ and Reynolds shear stresses $\overline{\rho}\,\widetilde{u''w''}$ are shown in figure 12. The magnitude of the normal-stress maximum decreases with increasing

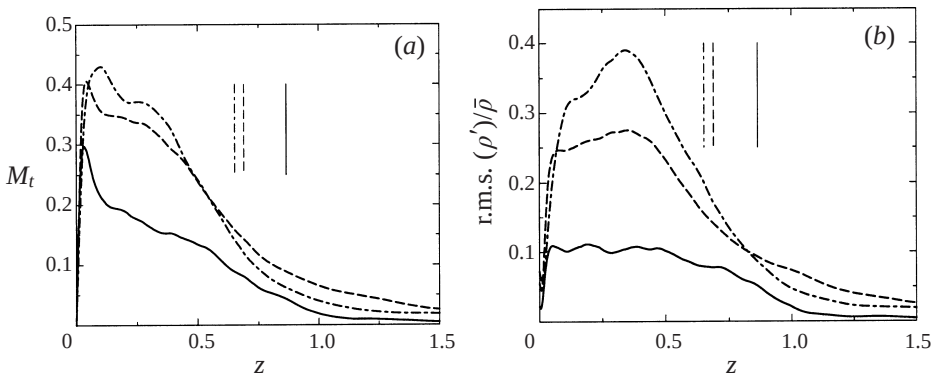

FIGURE 11. (*a*) Turbulent Mach number M_t; (*b*) r.m.s. $(\rho')/\bar{\rho}$; ——, case A; – – –, case B; — — —, case C. The vertical lines indicate the respective boundary-layer edges.

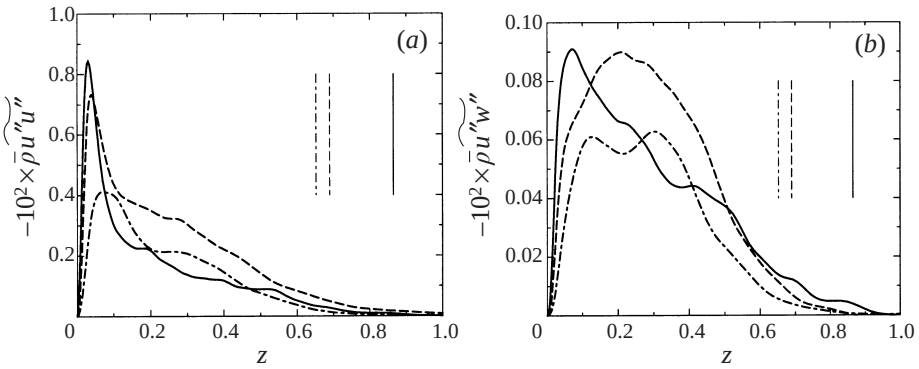

FIGURE 12. (*a*) Reynolds normal stress $\bar{\rho}\widetilde{u''u''}$; (*b*) Reynolds shear stress $-\bar{\rho}\widetilde{u''w''}$. ——, case A; – – –, case B; — · —, case C. The vertical lines indicate the respective boundary-layer edges.

Mach number. The maximum shear stress also diminishes with increasing Mach number and the profiles change their form. Case A displays a relatively sharp extremum close to the wall, which becomes flatter and moves away from the wall in case B. In case C, a double-peak form appears, where the second peak is located at the lower end of the wake region. This double peak vanishes for the Favre-averaged velocity-fluctuation correlation $\widetilde{u''w''}$. Although some experimental data show a double-peak profile as well (see e.g. Laderman & Demetriades 1979), it remains to be assessed whether this is an artifact of our simulation caused by the relatively short domain in case C.

In figure 13, the Reynolds stresses $\bar{\rho}\widetilde{u''u''}$ and $\bar{\rho}\widetilde{u''w''}$ are normalized with wall values and compared with the incompressible flat-plate simulation data of Spalart (1988) and the incompressible channel-flow data of Moser, Kim & Mansour (1999). The wall scaling almost collapses the Reynolds stresses for the supersonic channel flow (Huang *et al.* 1995). For the boundary layer, the extrema of the rescaled normal stresses assume values between 7 and 9.5. The compressible profiles have a similar shape to the incompressible profiles, though they are fuller in the wake region for the higher Mach numbers. No consistent trend is found for the rescaled shear stresses. The data of Spalart (1988) compare reasonably well with case A, while the channel-flow data obviously behave differently in the outer layer owing to the non-zero mean streamwise pressure gradient.

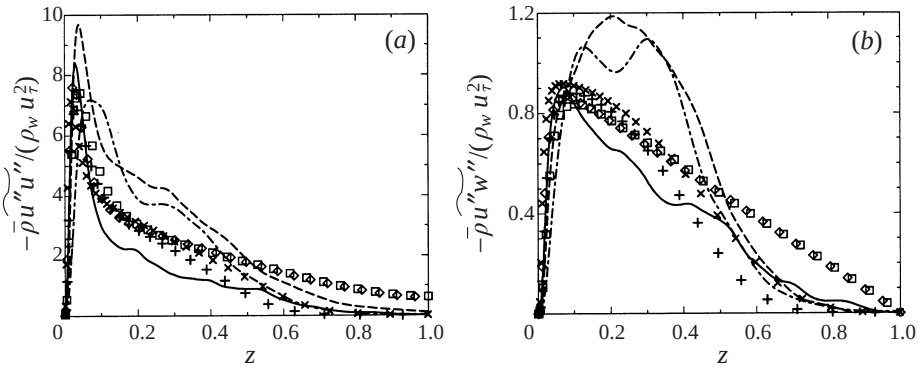

FIGURE 13. (*a*) Normalized Reynolds normal stress $\widetilde{\bar{\rho}u''u''}/(\rho_w u_\tau^2)$; (*b*) normalized Reynolds shear stress $-\widetilde{\bar{\rho}u''w''}/(\rho_w u_\tau^2)$. ——, case A; – – –, case B; — · —, case C; +, Spalart (1988), $Re_\theta = 670$; ×, Spalart, $Re_\theta = 1410$; □, Moser *et al.* (1999), $Re_\tau = 395$; ◇ Moser *et al.* (1999), $Re_\tau = 590$.

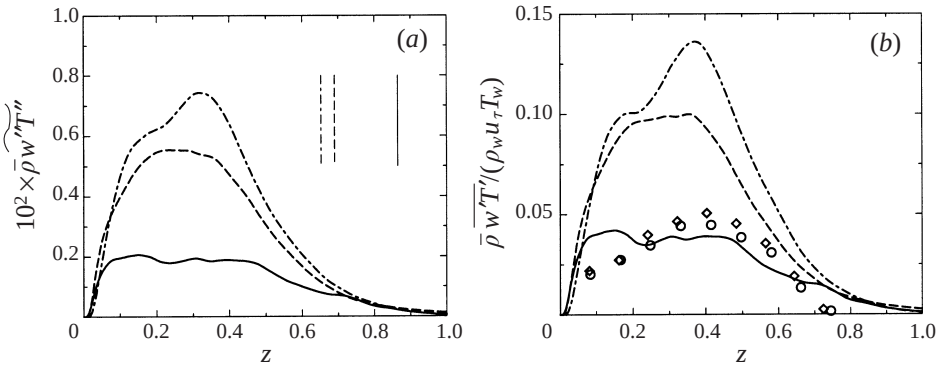

FIGURE 14. (*a*) Reynolds heat flux $\widetilde{\bar{\rho}w''T''}$ (the vertical lines indicate the respective boundary-layer edges). (*b*) Normalized Reynolds heat flux. ——, case A; – – –, case B; — · —, case C; ◯, 7306S0101; ◇, 7306S0102. The reference length for the experimental data was determined from a best fit with the computational data.

The Reynolds heat fluxes $\widetilde{\bar{\rho}w''T''}$ are shown in figure 14(*a*). The profile is relatively flat for case A, but develops a peak in the outer layer with increasing Mach number, unlike the profiles of $\widetilde{w''T''}$ which exhibit an extremum in the overlap layer. In figure 14(*b*) the heat fluxes $\overline{\bar{\rho}w'T'}$ normalized with wall values are compared with available experimental data at $M_\infty = 3.9$. This normalization does not collapse the data at all. The extrema of Rose's experimental data (7306S0101 and 7306S0102) are between those of cases A and B. The shape of the experimental profiles corresponds to what can be expected as a trend from case A to case B.

Experimental measurements of turbulent fluctuations in supersonic boundary-layer flows, particularly close to the wall, still pose considerable difficulties. The upstream history of the flow and the peculiarities of turbulence triggering (if employed) can significantly affect the form of the measured turbulent profiles. For comparison, we show in figure 15 the normalized Reynolds shear stresses $\overline{\bar{\rho}u'w'}$ for our and Spalart's numerical simulations and several experimental cases. Although the magnitude of the maxima is approximately consistent for all cases, the shapes of the profiles vary strongly. The data of Kussoy and Horstman (7802S0101 and 7802S0102) exhibit a

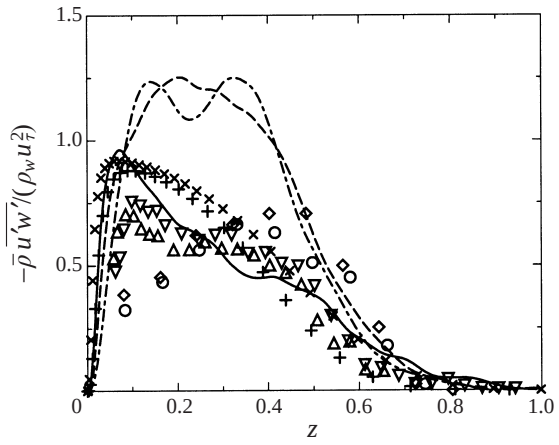

FIGURE 15. Scaled Reynolds shear stress $\bar{\rho}\,\overline{u'w'}/(\bar{\rho}_w u_\tau^2)$. ——, case A; – – –, case B; — · —, case C; +, Spalart (1988), $Re_\theta = 670$; ×, Spalart, $Re_\theta = 1410$; ○, 7306S0101; ◇, 7306S0102; △, 7802S0101; ▽, 7802S0102. The reference length for the experimental data was determined from a best fit with the computational data.

double-peak structure, not quite as pronounced as in our case C, whereas Rose's (7306S0101 and 7306S0102) and Spalart's data do not show a double peak. Similarly to our case B, Rose's data exhibit a plateau around the extremum, which is in contrast to Spalart's data and our case A where the peak is much sharper.

The following discussion about the double-peak structure of the Reynolds shear stress $\bar{\rho}\,\widetilde{u''w''}$ and $\bar{\rho}\,\overline{u'w'}$ may help to reconcile the somehow contradictory observations. Since we note an outward shift of the Reynolds-shear stress maximum with increasing Mach number, the double peak may appear in a transient Mach-number regime between lower M_∞, where the maximal turbulent activity is located in the buffer region, and higher M_∞, where the high-viscosity and low-density region close to the wall has pushed the turbulence activity up towards the mid-boundary layer. This concerns the velocity fluctuations less than the density and static temperature fluctuations. The following numerical data also demonstrate this upward displacement of the fluctuation maximum with increasing Mach number: density fluctuations (figure 11*b*), Reynolds heat flux (figure 14), temperature fluctuations (figure 18) and fluctuating Mach number. Experimental data support the above-mentioned trend, e.g. the measurements of Laderman & Demetriades (1979) in boundary layers at $M_\infty = 3$, 7.1 and 9.4. Our numerical data further show that in the mean x-momentum equation, where the z-derivative of the Reynolds shear stress $\overline{\rho u''w''}$ is involved, the terms $\partial(\bar{\rho}\tilde{u}^2)/\partial x$ and $\partial(\bar{\rho}\tilde{u}\tilde{w})/\partial z$ have their extremum at the z-position which corresponds to the location in the mid-boundary layer with increased turbulent activity. The effect of the Reynolds-number variation remains to be assessed.

3.3.2. *Turbulent-kinetic-energy balance*

The balance equation of turbulent kinetic energy $\bar{\rho}K$ in a compressible flow can be written as:

$$\frac{\partial \bar{\rho}K}{\partial t} = \underbrace{-\frac{\partial}{\partial x_j}(\bar{u}_j \bar{\rho} K)}_{\text{I}} + \underbrace{\bar{\rho}\tilde{\mathscr{P}}}_{\text{II}} + \underbrace{\bar{\rho}\Pi^{dl}}_{\text{III}} + \underbrace{\mathscr{M}}_{\text{IV}} + \underbrace{\frac{\partial \bar{\rho}\tilde{\mathscr{D}}_j^t}{\partial x_j}}_{\text{V}} \underbrace{-\bar{\rho}\varepsilon}_{\text{VI}} + \underbrace{\frac{\partial}{\partial x_j}\left(\frac{\bar{\mu}}{Re}\frac{\partial K}{\partial x_j}\right)}_{\text{VII}}. \tag{3.4}$$

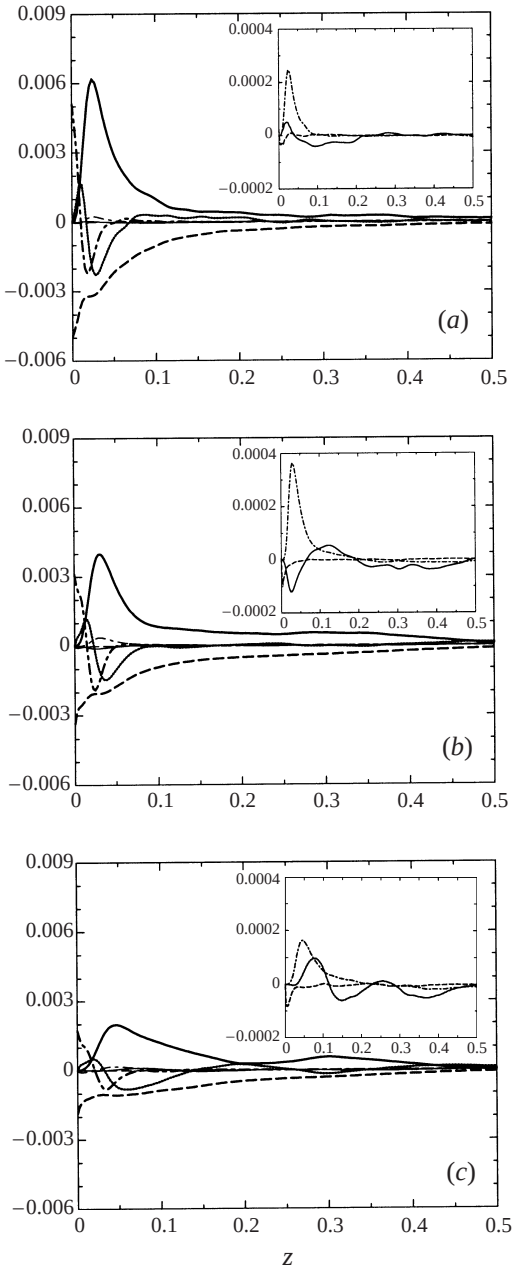

FIGURE 16. Turbulent-kinetic-energy budget equation (3.4): ——, I; ——, II; – – –, III; ——, IV; · · ·, V; – – –, VI; —·—, VII; (*a*) case A; (*b*) case B; (*c*) case C. The insets show a zoom of curves I, III and IV.

The following interpretations can be assigned to the individual terms of equation (3.4) whose detailed definition is given by Gatski (1997): I, turbulence convection; II, turbulence production; III, pressure dilatation; IV, mass flux variation; V, turbulent diffusion; VI, turbulent dissipation; VII, viscous diffusion. Figure 16 shows terms I to VII for the different cases A, B, and C, respectively. We observe that terms I, III

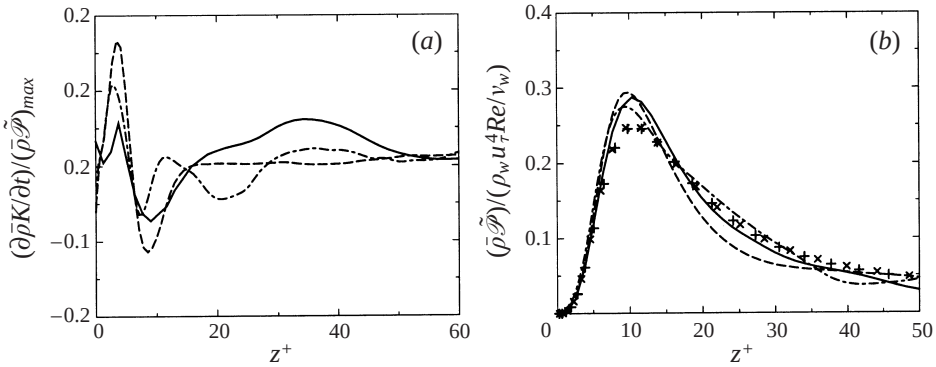

FIGURE 17. (*a*) Normalized mean time-derivative of the TKE; (*b*) normalized turbulence production. ——, case A; – – –, case B; ——, case C; +, Spalart (1988), $Re_\theta = 670$; ×, Spalart, $Re_\theta = 1410$.

and IV are almost negligible. Turbulence production (II), turbulent dissipation (VI), viscous diffusion (VII) and turbulent diffusion (V) reduce significantly with increasing Mach number. From DNS of homogeneous turbulent shear flow, Sarkar (1995) found that the main effect of compressibility is to reduce turbulence production. This finding has been confirmed for supersonic mixing layers by Vreman, Sandham & Luo (1996), for supersonic channel flows by Huang *et al.* (1995), and is corroborated by our boundary-layer data.

In a fully developed flow, at a given spatial station, the turbulent kinetic energy (TKE) has reached its equilibrium level, so that its time derivative goes to zero. Evaluating this time derivative with equation (3.4) reveals that the residual for our data is still of the same order of magnitude as the above-mentioned small terms (convection, pressure dilatation, mass flux variation). However, if this mean TKE time-derivative is scaled with the maximum turbulence production, it can be seen in figure 17(*a*) that $\partial\bar{\rho}K/\partial t$ is still reasonably small within the active turbulent region. Nevertheless, the dominant terms (II, V, VI and VII) compare well with the incompressible data of Spalart (1988) when scaled with the skin-friction velocity, the density and viscosity at the wall. This is illustrated in figure 17(*b*) for the turbulence production $\bar{\rho}\tilde{\mathscr{P}}$. Note that in Huang *et al.* (1995), where the channel walls are cooled, a mixed scaling with inner and outer variables is used to collapse incompressible and compressible data sets.

3.3.3. *Reynolds analogy*

An important issue in supersonic turbulent boundary layers is the validity of the strong Reynolds analogy (SRA), which in its strict form means a perfect negative correlation between T'' and u''. The SRA can be derived from the linearized equation

$$\frac{T_0''}{\tilde{T}} \doteq \frac{T''}{\tilde{T}} + (\gamma - 1)M_\infty^2 \frac{\tilde{u}\,u''}{\tilde{T}}$$

under the assumption of negligible total temperature fluctuations $T_0''/\tilde{T}$ (Lele 1994). After some algebra (note that $\tilde{M} = \tilde{u}/\tilde{a}$ is the local Mach number)

$$\frac{T''}{\tilde{T}} = -(\gamma - 1)\tilde{M}^2 \frac{u''}{\tilde{u}} \tag{3.5}$$

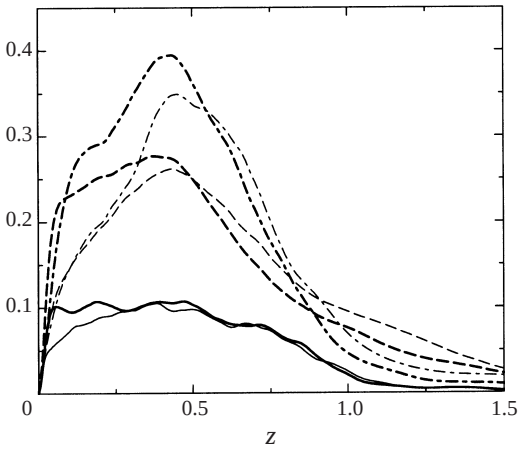

FIGURE 18. Thick lines r.m.s. $(T'')/\tilde{T}$, thin lines r.m.s. $(T_0'')/\tilde{T}$, ——, case A; – – –, case B; — – —, case C.

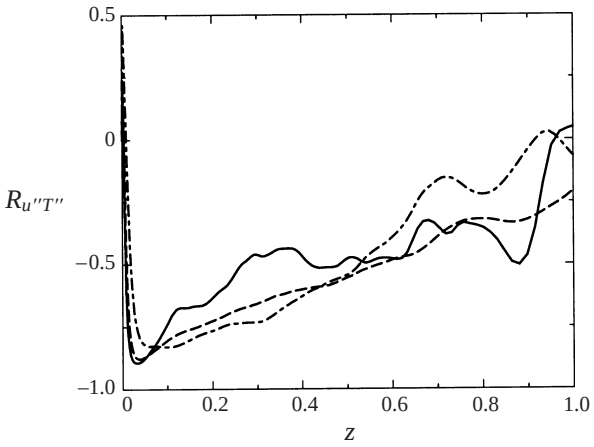

FIGURE 19. Correlation coefficient $R_{u''T''}$; ——, case A; – – –, case B; — – —, case C.

is obtained and by this relation the correlation coefficient

$$R_{u''T''} := \frac{\overline{u''T''}}{\text{r.m.s.}\,(u'')\,\text{r.m.s.}\,(T'')} = -1. \tag{3.6}$$

It can be seen in figure 18 that r.m.s. $(T_0'')/\tilde{T}$ is practically of the same magnitude as r.m.s. $(T'')/\tilde{T}$. Thus, the assumption $T_0''/\tilde{T} \ll T''/\tilde{T}$ used to derive equations (3.5) and (3.6) is not justified. As can be seen in figure 19, relation (3.6) is not well satisfied for all our cases A, B and C. The data show that $R_{u''T''}$ is close to about -0.8 just above the sublayer, but decreases in magnitude to a value near zero towards the boundary-layer edge. In the outer part of the boundary layer, the SRA is not valid with acceptable accuracy. In fact, the $R_{u''T''}$ profiles rather show a similarity with low-Mach-number experimental results (Smits & Dussauge 1996 figure 5.5). Note also that a positive near-wall correlation has been found in the DNS of strongly cooled channel flow (Coleman *et al.* 1995). Other SRA relations for adiabatic boundary conditions were presented by Morkovin (1962). By taking the root-mean-square of

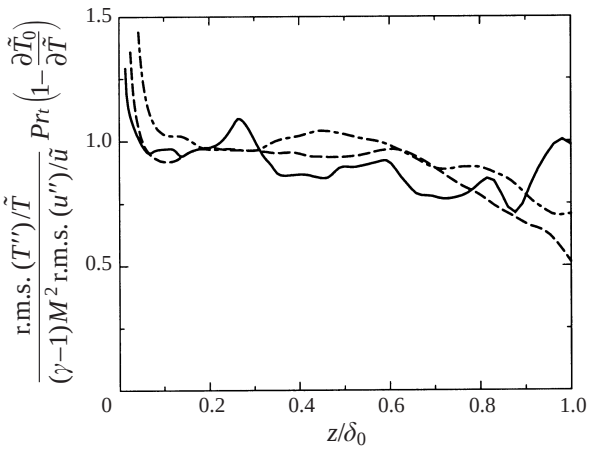

FIGURE 20. Formulation of the SRA proposed by Huang *et al.* (1995); ——, case A; – – –, case B; — — —, case C.

equation (3.5), we obtain:

$$\frac{(\text{r.m.s.}\,(T'')/\tilde{T})}{(\gamma-1)\,\tilde{M}^2\,(\text{r.m.s.}\,(u'')/\tilde{u})} \approx 1. \tag{3.7}$$

This relation can be extended to take heat flux at the wall into account. Huang *et al.* (1995) propose the following formulation which gives better results than (3.7), but still shows an error of up to 20% for supersonic channel flow:

$$\frac{(\text{r.m.s.}\,(T'')/\tilde{T})}{(\gamma-1)\,\tilde{M}^2(\text{r.m.s.}\,(u'')/\tilde{u})}\,Pr_t\left(1-\frac{\partial\tilde{T}_0}{\partial\tilde{T}}\right) \approx 1 \tag{3.8}$$

where Pr_t is the turbulent Prandtl number

$$Pr_t = \frac{\overline{\rho w'' u''}}{\overline{\rho w'' T''}}\,\frac{\partial\tilde{T}/\partial z}{\partial\tilde{u}/\partial z}. \tag{3.9}$$

Figure 20 shows that the prediction by equation (3.8) is in better agreement with the simulation data than (3.6) in the bulk of the boundary layer, but the agreement degrades towards the boundary-layer edge. We note, however, that for ETDNS results with non-adiabatic wall conditions (Maeder 2000), equation (3.8) shows a considerable improvement over equation (3.7) if there is a significant mean heat flux across the wall.

3.3.4. *Compressibility effects on dissipation and pressure–strain*

In equation (3.4), not all terms which arise for compressible flow have been spelled out. One is the pressure dilatation

$$\bar{\rho}\Pi^{dl} = \overline{p'\,\frac{\partial u_i''}{\partial x_i}}, \tag{3.10}$$

which is the trace of the pressure–strain tensor and represents a transfer between internal energy and turbulent kinetic energy. As can be seen from the channel flow data of Huang *et al.* (1995), $\bar{\rho}\Pi^{dl}$ is negative in the wall vicinity, resulting in a transfer of kinetic to internal energy, then it assumes a small positive value and finally approaches zero in the middle part of the channel. A similar behaviour can be

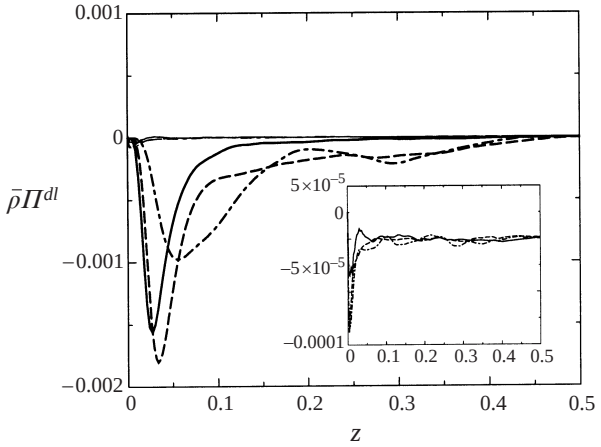

FIGURE 21. Pressure dilatation $\bar{\rho}\Pi^{dl}$ from DNS (upper curves) and predictions of model (3.11) (lower curves); the inset shows a zoom of the upper curves; ——, case A; – – –, case B; ——–, case C.

observed for our DNS data in figure 21. For illustration, we have also plotted data from a model proposed for free shear layers by El Baz & Launder (1993),

$$\bar{\rho}\Pi^{dl} = 3\bar{\rho}M_t^2\left(\frac{4}{3}K\frac{\partial\tilde{u}_i}{\partial x_i} - \tilde{\mathscr{P}}\right). \tag{3.11}$$

The model considerably overpredicts turbulent kinetic energy losses by pressure dilatation and is not suitable for wall-bounded flows.

Another term arising from the non-vanishing velocity-divergence is the dilatational dissipation

$$\bar{\rho}\varepsilon_d = \frac{4}{3}\frac{\bar{\mu}}{Re}\overline{\frac{\partial u_i''}{\partial x_i}\frac{\partial u_i''}{\partial x_i}}. \tag{3.12}$$

The solenoidal dissipation is commonly defined as

$$\bar{\rho}\varepsilon_s = \frac{\bar{\mu}}{Re}\overline{\omega_i''\omega_i''}, \tag{3.13}$$

and the total dissipation is

$$\bar{\rho}\varepsilon = \overline{\tau_{ik}'\frac{\partial u_i'}{\partial x_k}}. \tag{3.14}$$

For the three cases A, B, and C, $\varepsilon_d/\varepsilon$ and $\varepsilon_d/\varepsilon_s$ are shown in figure 22. The ratios increase by nearly one order of magnitude for cases A to C. For all cases, $\bar{\rho}\varepsilon_d$ is more than one order of magnitude smaller than $\bar{\rho}\varepsilon$ and about of the same magnitude as $\bar{\rho}\Pi^{dl}$. The initial level of ϵ_d/ϵ_s for homogeneous shear flow at $M_{\text{r.m.s.}} = 0.3$ and shear rate $S = 1.53$ (Blaisdell, Mansour & Reynolds 1993) is comparable to our case C. The profile of $\varepsilon_d/\varepsilon_s$ in case B of Huang *et al.* (1995) compares well with our case A, despite the different wall-temperature conditions.

Present modelling approaches for the dilatational dissipation can generally be cast into the form (Gatski 1997)

$$\varepsilon_d = \alpha\mathscr{F}(M_t)\varepsilon_s\ , \tag{3.15}$$

where ε_s can be replaced by $\varepsilon - \varepsilon_d$, $|\varepsilon - \varepsilon_s|$ being small as figure 22 shows. Different

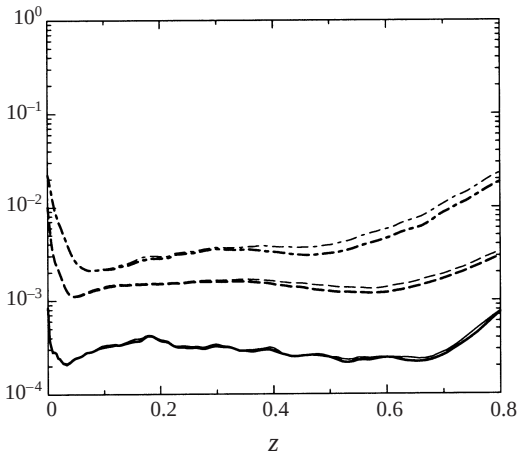

FIGURE 22. Ratio of dilatational dissipation to total and solenoidal dissipation, respectively. Thick lines $\varepsilon_d/\varepsilon$, thin lines $\varepsilon_d/\varepsilon_s$; ——, case A; – – –, case B; — — —, case C.

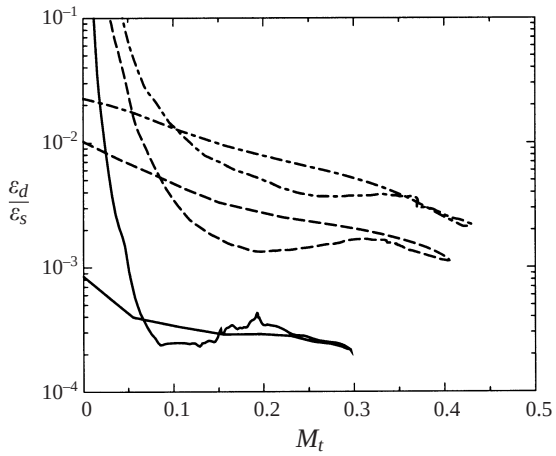

FIGURE 23. $\varepsilon_d/\varepsilon_s$ over M_t; ——, case A; – – –, case B; — — —, case C.

functions $\mathscr{F}(M_t)$ have been proposed and have been summarized by Gatski (1997). The simplest form is $\mathscr{F}(M_t) = M_t^2$, derived from homogeneous turbulence data. Huang *et al.* (1995) found that the simple form of equation (3.15) fails for turbulent channel flows. Figure 23 shows ϵ_d/ϵ_s as a function of the turbulent Mach number M_t. The figure indicates a weak exponential dependence of $\varepsilon_d/\varepsilon_s$ on M_t in the lower part of the boundary layer. In the outer part of the boundary layer the dependence resembles $\sim \exp(1/M_t)$. The overall level apparently depends on M_∞. There is no simple functional relationship between $\varepsilon_d/\varepsilon_s$ and M_t, as figure 23 shows. For a successful modelling of $\varepsilon_d/\varepsilon_s$ in a boundary layer, other parameters have to enter the model.

In his study of dilatational covariances in compressible turbulence, Ristorcelli (1997) found that in isotropic turbulence the ratio of dilatational dissipation to solenoidal dissipation scales with M_t^4/R_t (where R_t is the turbulent Reynolds number). In order to find a more globally valid relationship, we define a mean ratio $\overline{\epsilon_d/\epsilon_s}$ in the boundary

layer:

$$\overline{\left(\frac{\epsilon_d}{\epsilon_s}\right)} = \frac{1}{\delta_0}\int_0^{\delta_0} \frac{\epsilon_d}{\epsilon_s}\mathrm{d}z. \tag{3.16}$$

We found empirically that this ratio scales roughly with

$$\overline{\left(\frac{\epsilon_d}{\epsilon_s}\right)} \sim \frac{M_\infty^{3.4}}{Re_\theta} \tag{3.17}$$

which bears some resemblance to Ristorcelli's scaling, however, being expressed in global flow parameters. This relation shows that ϵ_d/ϵ_s indeed becomes small for increasing Reynolds numbers, but also that this trend is much weaker for higher Mach numbers.

4. Summary and concluding remarks

We have formulated an extended temporal direct numerical simulation (ETDNS) model which allows, on the basis of an existing TDNS method, for the accurate simulation of spatially developing boundary layers. The ETDNS approach approximates well a spatially evolving turbulent boundary layer, while it requires one to two orders of magnitude less computing resources than a comparable fully spatial simulation. We have used this approach to simulate zero-pressure-gradient flat-plate boundary layers for three cases at free-stream Mach numbers $M_\infty = 3$, 4.5 and 6 with the objective of investigating the compressibility effects and turbulence structure.

Comparison with experimental data shows an excellent agreement between the mean flow obtained from the simulation and the experiments. We find that, in agreement with channel-flow simulations of Coleman *et al.* (1995), compressibility effects on turbulence statistics are small up to a Mach number of about 5, but seem to grow in importance for higher M_∞. The fact that the van Driest transformed velocity profiles compare well with the incompressible law of the wall, that the structure parameter has approximately the same value for compressible and incompressible boundary layers, and that the intrinsic compressibility effects remain small, tends to confirm the validity of Morkovin's hypothesis. However, we have seen that for $M_\infty \gtrsim 5$ the relative density fluctuations become important in the outer part of the boundary layer, causing the Favre and Reynolds average of the static temperature to differ. Also, there are indications that the shape of the Reynolds shear stress profile changes. The total temperature fluctuations cannot be neglected (not even for $M_\infty = 3$), which invalidates many of the assumptions made in deriving the strong Reynolds analogy. Thus, the predicted perfect anticorrelation between u'' and T'' ($R_{u''T''} = -1$) is not corroborated. Nevertheless, some alternative or extended formulations perform reasonably well. Modelling approaches, which so far are based mainly on homogeneous turbulence DNS data, fail to predict compressibility effects in boundary layers correctly.

T. M. was supported by a doctoral fellowship granted by the Swiss ERCOFTAC Pilot Centre. N. A. A. acknowledges support by CRAY Research, Inc., and the Swiss National Science Foundation. Computations have been performed at the Swiss Center for Scientific Computing CSCS in Manno. The support of the CSCS staff, in particular M. Ballabio and the NEC/CSCS task force, for the code parallelization and optimization is gratefully acknowledged.

Appendix. Extended temporal direct numerical simulation approach

A.1. *Solving the Reynolds-averaged equations for mean-flow quantities within a TDNS*

As an example, and for simplicity, we first demonstrate the approach for an incompressible flow. The flow field can be decomposed as $\boldsymbol{u} = \bar{\boldsymbol{u}} + \boldsymbol{u}'$, where $\bar{\boldsymbol{u}}$ represents the mean flow and the term $\boldsymbol{u}'$ represents the remaining fluctuating part. The governing equations for $\bar{\boldsymbol{u}}$ are the Reynolds–averaged Navier–Stokes equations:

$$\nabla \cdot \bar{\boldsymbol{u}} = \boldsymbol{0}, \tag{A 1}$$

$$\nabla \cdot (\bar{\boldsymbol{u}} \otimes \bar{\boldsymbol{u}}) = -\nabla \bar{p} + \frac{1}{Re} \nabla^2 \bar{\boldsymbol{u}} - \nabla \cdot (\overline{\boldsymbol{u}' \otimes \boldsymbol{u}'}), \tag{A 2}$$

where we write briefly $\overline{\boldsymbol{u}' \otimes \boldsymbol{u}'}$ for the Reynolds stresses (an overbar represents an averaged quantity). In boundary layers, $\bar{\boldsymbol{u}}$ usually varies slowly in the streamwise direction, and the governing equations (A 1) and (A 2) can be parabolized by dropping the ∂_x derivatives in the diffusive term,

$$\nabla \cdot \bar{\boldsymbol{u}} = \boldsymbol{0}, \tag{A 3}$$

$$\nabla \cdot (\bar{\boldsymbol{u}} \otimes \bar{\boldsymbol{u}}) = -\nabla \bar{p} + \frac{1}{Re} \nabla_P^2 \bar{\boldsymbol{u}} - \nabla \cdot (\overline{\boldsymbol{u}' \otimes \boldsymbol{u}'}), \tag{A 4}$$

where $\nabla_P = \{0, \partial/\partial y, \partial/\partial z\}$. The equations require closure for the unknown Reynolds stresses $\overline{\boldsymbol{u}' \otimes \boldsymbol{u}'}$ in equation (A 4).

In a conventional TDNS approach, the actual equations for the mean flow $\bar{\boldsymbol{u}}$ are:

$$\nabla_P \cdot \bar{\boldsymbol{u}} = \boldsymbol{0}, \tag{A 5}$$

$$\frac{\partial \bar{\boldsymbol{u}}}{\partial t} + \nabla_P \cdot (\bar{\boldsymbol{u}} \otimes \bar{\boldsymbol{u}}) = -\nabla_P \bar{p} + \frac{1}{Re} \nabla_P^2 \bar{\boldsymbol{u}} - \nabla_P \cdot (\overline{\boldsymbol{u}' \otimes \boldsymbol{u}'}). \tag{A 6}$$

Note that here $\bar{\boldsymbol{u}}$ is a function of time and an overbar represents a quantity which has been spatially averaged over x. We introduce the slow streamwise scale $\xi = \epsilon x$, where $0 < \epsilon \ll 1$. If we compare equations (A 3) and (A 4) with equations (A 5) and (A 6), invoking ergodicity to replace Reynolds averages by spatial averages, we note that the following terms are missing from the right-hand sides of equations (A 5) and (A 6):

$$\boldsymbol{Z}_{0_S} = \begin{bmatrix} -\dfrac{\partial \bar{u}}{\partial \xi} \\ -\dfrac{\partial \bar{u}\bar{u}}{\partial \xi} - \dfrac{\partial \bar{p}}{\partial \xi} - \dfrac{\partial \overline{u'u'}}{\partial \xi} \\ -\dfrac{\partial \bar{u}\bar{v}}{\partial \xi} - \dfrac{\partial \overline{u'v'}}{\partial \xi} \\ -\dfrac{\partial \bar{u}\bar{w}}{\partial \xi} - \dfrac{\partial \overline{u'w'}}{\partial \xi} \end{bmatrix}. \tag{A 7}$$

Equations (A 5) and (A 6), with terms (A 7) added, constitute a transient problem of equations (A 3) and (A 4). The solutions of these equations converges to those of the original equations if $\partial \bar{\boldsymbol{u}}/\partial t \to 0$. Note that the streamwise variations of the Reynolds-stress terms are also included in equation (A 7).

At each station $\xi = \xi_{n+1}$, the solution of the full equations with $\boldsymbol{Z}_{0_S}$ added is integrated in time until a steady state is reached. Then, the solution is marched downstream to the next station $\xi = \xi_{n+2}$. For the approximation of the derivatives on

the slow streamwise scale, a second-order backward-difference formula is used:

$$\left.\frac{\partial(\bullet)}{\partial\xi}\right|_{\xi_{n+1}} = \frac{1}{\xi_{n+1}-\xi_n}\left[\frac{1+2\omega_n}{1+\omega_n}(\bullet)_{n+1} - (1+\omega_n)(\bullet)_n + \frac{\omega_n^2}{1+\omega_n}(\bullet)_{n-1}\right], \tag{A 8}$$

where $\omega_n = (\xi_{n+1}-\xi_n)/(\xi_n-\xi_{n-1})$.

A.2. *Non-parallel effects*

We notice that the terms of equation (A 7) which contain mean-flow derivatives account for mean-flow non-parallelism. The interaction of mean-flow non-parallelism with the locally fluctuating flow $\boldsymbol{u}'$ has not been considered yet, as the following example shows. If we look at the nonlinear term $\partial uu/\partial x$ and split $u = \bar{u} + u'$ into its mean and fluctuating part, where $\partial\bar{u}/\partial x = 0$, but $\partial\bar{u}/\partial\xi \neq 0$, we obtain by also introducing the relevant dependencies

$$\frac{\partial(\bar{u}(\xi)+u'(x))(\bar{u}(\xi)+u'(x))}{\partial x} = 2\epsilon\bar{u}\dot{\bar{u}} + 2\epsilon u'\dot{\bar{u}} + 2\bar{u}\dot{u}' + 2u'\dot{u}'. \tag{A 9}$$

Here, we have used $\xi = \epsilon x$ as defined previously and a dot to indicate the derivative with respect to the argument. If we now use $\partial\bar{u}/\partial x = 0$ and collect terms we obtain

$$\frac{\partial(\bar{u}(\xi)+u'(x))(\bar{u}(\xi)+u'(x))}{\partial x} = \frac{\partial\bar{u}\bar{u}}{\partial\xi} + \frac{\partial uu}{\partial x} + 2u'\frac{\partial\bar{u}}{\partial\xi}.$$

We recognize that the first term is part of $\boldsymbol{Z}_{0_S}$, equation (A 7), the second term is part of the locally solved Navier–Stokes equations and only the third term, which represents the interaction of mean-flow non-parallelism and local fluctuations, is missing. If we carry out the same analysis for all relevant terms, we obtain the following expression which must be added to the locally solved Navier–Stokes equations in order to take these interactions into account:

$$\boldsymbol{Z}_{1_S} = \begin{bmatrix} 0 \\ -2(u-\bar{u})\dfrac{\partial\bar{u}}{\partial\xi} \\ -(u-\bar{u})\dfrac{\partial\bar{v}}{\partial\xi} - (v-\bar{v})\dfrac{\partial\bar{u}}{\partial\xi} \\ -(u-\bar{u})\dfrac{\partial\bar{w}}{\partial\xi} - (w-\bar{w})\dfrac{\partial\bar{u}}{\partial\xi} \end{bmatrix}. \tag{A 10}$$

We note that the term $\boldsymbol{Z}_{1_S}$ is equivalent to the forcing term $\boldsymbol{Z}_1$ in Guo, Adams & Kleiser (1995), and it only acts on the governing equations for $\boldsymbol{u}'$.

A.3. *Extension to compressible flow*

In the case of compressible boundary-layer flows, the governing equations to be solved can be written as

$$\frac{\partial\boldsymbol{U}}{\partial t} = \frac{\partial\boldsymbol{F}}{\partial x} + \frac{\partial\boldsymbol{G}}{\partial y} + \frac{\partial\boldsymbol{H}}{\partial z} + \boldsymbol{Z}_0 + \boldsymbol{Z}_1. \tag{A 11}$$

The term $\boldsymbol{Z}_0$ is derived in the same way as $\boldsymbol{Z}_{0_s}$ described above, equation (A 7). It has the form

$$\boldsymbol{Z}_0 = \frac{\partial}{\partial \xi}\begin{bmatrix} -\overline{\rho u} \\ -\overline{\rho u^2} - \bar{p} + \overline{\tau_{xx}} \\ -\overline{\rho u v} + \overline{\tau_{xy}} \\ -\overline{\rho u w} + \overline{\tau_{xz}} \\ -\overline{u(E+p)} - \overline{q_x} + \overline{u\tau_{xx}} + \overline{v\tau_{xy}} + \overline{w\tau_{xz}} \end{bmatrix} + \boldsymbol{Z}_m, \tag{A 12}$$

where τ_{xx}, τ_{xy}, and τ_{xz} are the components of the shear-stress tensor and q_x is the heat flux component in the x-direction. The term $\boldsymbol{Z}_m$ contains the other terms missing in equation (A 12) which drop out of the locally solved Navier–Stokes equations owing to the periodicity assumption in x. It has the form

$$\boldsymbol{Z}_m = \frac{1}{Re}\begin{bmatrix} 0 \\ \frac{4}{3}\frac{\partial\bar{\mu}}{\partial\xi}\frac{\partial\bar{u}}{\partial\xi} + \frac{\partial}{\partial y}\left(\bar{\mu}\frac{\partial\bar{v}}{\partial\xi}\right) + \frac{\partial}{\partial z}\left(\bar{\mu}\frac{\partial\bar{w}}{\partial\xi}\right) \\ \frac{\partial\bar{\mu}}{\partial\xi}\frac{\partial\bar{v}}{\partial\xi} - \frac{2}{3}\frac{\partial}{\partial y}\left(\bar{\mu}\frac{\partial\bar{u}}{\partial\xi}\right) \\ \frac{\partial\bar{\mu}}{\partial\xi}\frac{\partial\bar{w}}{\partial\xi} - \frac{2}{3}\frac{\partial}{\partial z}\left(\bar{\mu}\frac{\partial\bar{u}}{\partial\xi}\right) \\ \frac{1}{(\kappa-1)M_\infty^2 Pr}\frac{\partial\bar{\mu}}{\partial\xi}\frac{\partial\bar{T}}{\partial\xi} + \frac{4}{3}\bar{\mu}\left(\frac{\partial\bar{u}}{\partial\xi}\right)^2 + \frac{4}{3}\bar{u}\frac{\partial\bar{\mu}}{\xi}\frac{\partial\bar{\mu}}{\partial\xi} + \\ +\bar{\mu}\left(\frac{\partial\bar{v}}{\partial\xi}\right)^2 + \bar{v}\frac{\partial\bar{\mu}}{\partial\xi}\frac{\partial\bar{v}}{\partial\xi} + \bar{\mu}\left(\frac{\partial\bar{w}}{\partial\xi}\right)^2 + \bar{w}\frac{\partial\bar{\mu}}{\partial\xi}\frac{\partial\bar{w}}{\partial\xi} + \\ +\frac{\partial}{\partial y}\left(\bar{\mu}\bar{u}\frac{\partial\bar{v}}{\partial\xi}\right) - \frac{2}{3}\frac{\partial}{\partial y}\left(\bar{\mu}\bar{v}\frac{\partial\bar{u}}{\partial\xi}\right) + \frac{\partial}{\partial z}\left(\bar{\mu}\bar{u}\frac{\partial\bar{w}}{\partial\xi}\right) - \frac{2}{3}\frac{\partial}{\partial z}\left(\bar{\mu}\bar{w}\frac{\partial\bar{u}}{\partial\xi}\right) \end{bmatrix}. \tag{A 13}$$

For a zero-pressure-gradient boundary layer over a flat plate, we set $\partial\bar{p}/\partial\xi$ to zero. The term $\boldsymbol{Z}_1$ in equation (A 11) is given by

$$\boldsymbol{Z}_1 = \begin{bmatrix} -\rho\frac{\partial\bar{u}}{\partial\xi} - u\frac{\partial\bar{\rho}}{\partial\xi} + \frac{\partial(\bar{\rho}\bar{u})}{\partial\xi} \\ -(u-\bar{u})\frac{\partial\overline{\rho u}}{\partial\xi} - (\rho u - \overline{\rho u})\frac{\partial\bar{u}}{\partial\xi} \\ -(u-\bar{u})\frac{\partial\overline{\rho v}}{\partial\xi} - (\rho v - \overline{\rho v})\frac{\partial\bar{u}}{\partial\xi} \\ -(u-\bar{u})\frac{\partial\overline{\rho w}}{\partial\xi} - (\rho w - \overline{\rho w})\frac{\partial\bar{u}}{\partial\xi} \\ -(u-\bar{u})\frac{\partial}{\partial\xi}(\bar{E}+\bar{p}) - (E+p-\bar{E}-\bar{p})\frac{\partial\bar{u}}{\partial\xi} \end{bmatrix}. \tag{A 14}$$

In order to validate the procedure, a laminar boundary-layer flow at $M_\infty = 4.5$ has been computed, with all non-zero streamwise Fourier modes set to be zero (i.e. the

Reynolds-stress terms are set to zero). Similarity solutions for the boundary layer are used as initial profiles to start the downstream spatial marching. At each spatial step, the solution is advanced in time until a steady state is reached. Once the steady state is reached, the solution is marched downstream by another step. At all spatial steps, the results replicate the similarity solutions accurately, which are indistinguishable from the full boundary-layer solutions.

REFERENCES

Adams, N. A. & Kleiser, L. 1996 Subharmonic transition to turbulence in a flat plate boundary layer at Mach number 4.5. *J. Fluid Mech.* **317**, 301–335.

Adams, N. A., Maeder, T., Guo, Y. & Kleiser, L. 2000 An extended temporal approach for the direct simulation of turbulent compressible boundary layers. Submitted.

Blaisdell, G. A., Mansour, N. N. & Reynolds, W. C. 1993 Compressibility effects on the growth and structure of homogeneous turbulent shear flow. *J. Fluid Mech.* **256**, 443–485.

Bradshaw, P. 1997 Compressible turbulent shear layers. *Ann. Rev. Fluid Mech.* **9**, 33–54.

Coleman, G. N., Kim, J. & Moser, R. D. 1995 A numerical study of turbulent supersonic isothermal-wall channel flow. *J. Fluid Mech.* **305**, 159–183.

El Baz, A. M. & Launder, B. E. 1993 Second-moment modelling of compressible mixing layers. In *Engineering Turbulence Modelling and Experiments 2* (ed. W. Rodi & F. Martelli). Elsevier.

Fernholz, H. H. & Finley, P. J. 1997 A critical compilation of compressible turbulent boundary layer data. *Tech. Rep.* AGARDograph 223. AGARD, Neuilly sur Seine, France.

Fernholz, H. H. & Finley, P. J. 1980 A critical commentary on mean flow data for two-dimensional compressible turbulent boundary layers. *Tech Rep.* AGARDograph 253. AGARD, Neuilly sur Seine, France.

Fernholz, H. H. & Finley, P. J. 1981 A further compilation of compressible boundary layer data with a survey of turbulence data. *Tech. Rep.* AGARDograph 263. AGARD, Neuilly sur Seine, France.

Friedrich, R. & Bertolotti, F. P. 1997 Compressibility effects due to turbulent fluctuations. *Appl. Sci. Res.* **57**, 165–194.

Gatski, T. B. 1997 Modelling compressibility effects on turbulence. In *New Tools in Turbulence Modelling* (ed. O. Métais & J. H. Ferziger), pp. 73–104. Springer.

Gaviglio, J. 1987 Reynolds analogies and experimental study of heat transfer in the supersonic boundary layer. *Intl J. Heat Mass Transfer* **30**, 911–926.

Guarini, S. E., Moser, R. D., Shariff, K. & Wray, A. 2000 Direct numerical simulation of a supersonic turbulent boundary layer at Mach 2.5. *J. Fluid Mech.* **414**, 1–33.

Guo, Y., Adams, N. A. & Kleiser, L. 1995 Modeling of nonparallel effects in temporal direct numerical simulations of compressible boundary-layer transition. *Theoret. Comput. Fluid Dyn.* **7**, 141–157.

Herbert, T. 1997 Parabolized stability equations. *Ann. Rev. Fluid Mech.* **29**, 245–283.

Huang, P. G., Coleman, G. N. & Bradshaw, P. 1995 Compressible turbulent channel flows: DNS results and modelling. *J. Fluid Mech.* **305**, 185–218.

Jimenez, J. & Moin, P. 1991 The minimal flow unit in near-wall turbulence. *J. Fluid Mech.* **225**, 213–240.

Kleiser, L. & Zang, T. 1991 Numerical simulation of transition in wall-bounded shear flows. *Ann. Rev. Fluid Mech.* **23**, 495–537.

Laderman, A. J. & Demetriades, A. 1979 Turbulent shear stress in compressible boundary layers. *AIAA J.* **17**(7), 736–744.

Lele, S. K. 1992 Compact finite difference schemes with spectral-like resolution. *J. Comput. Phys.* **103**, 16–42.

Lele, S. K. 1994 Compressibility effects on turbulence. *Ann. Rev. Fluid Mech.* **26**, 211–254.

Lund, T. S., Wu, X. & Squires, K. D. 1998 Generation of turbulent inflow data for spatially-developing boundary layer simulations. *J. Comput. Phys.* **140**, 233–258.

Luo, K. H. & Sandham, N. D. 1995 Direct simulation of scalar mixing in a compressible mixing layer. In *Proc. 5th European Turbulence Conf. Siena, Italy, 5–8 July 1994* (ed. R. Benzi), *Advances in Turbulence*, vol. 5, pp. 340–345. Kluwer.

Mack, L. M. 1984 Boundary-layer linear stability theory. In *Special Course on Stability and Transition of Laminar Flow, AGARD Rep.* 709, pp. 3-1–3-81.

Maeder, T. 2000 Numerical investigation of supersonic turbulent boundary layers. PhD thesis, ETH Zürich, Institute of Fluid Dynamics, Zürich, Switzerland, in preparation.

Morkovin, M. V. 1962 Effects of compressibility on turbulent flows. In *Mécanique de la Turbulence* (ed. A. Favre), pp. 367–380. CNRS, Paris.

Moser, R. D., Kim, J. & Mansour, N. N. 1999 Direct numerical simulation of turbulent channel flow up to $Re_r = 590$. *Phys. Fluids* **11**, 943–945.

Rai, M. M., Gatski, T. B. & Erlebacher, G. 1995 Direct simulation of spatially evolving compressible turbulent boundary layers. *AIAA Paper* 95-0583.

Ristorcelli, J. R. 1997 A pseudo-sound constitutive relationship for the dilatational convariances in compressible turbulence. *J. Fluid Mech.* **347**, 37–70.

Sarkar, S. 1995 The stabilizing effect of compressibility in turbulent shear flow. *J. Fluid Mech.* **282**, 163–186.

Smits, A. J. & Dussauge, J.-P. 1996 *Turbulent Shear Layers in Supersonic Flow*. AIP Press, Woodbury, New York.

Spalart, P. R. 1988 Direct simulation of a turbulent boundary layer up to $Re_\theta = 1410$. *J. Fluid Mech.* **187**, 61–98.

Thompson, K. W. 1987 Time dependent boundary conditions for hyperbolic systems. *J. Comput. Phys.* **68**, 1–24.

Vreman, A. W., Sandham, N. D. & Luo, K. H. 1996 Compressible mixing layer growth rate and turbulence characteristics. *J. Fluid Mech.* **320**, 235–258.

Williamson, J. H. 1980 Low-storage Runge–Kutta schemes. *J. Comput. Phys.* **35**, 48–56.

Wray, A. & Hussaini, M. Y. 1984 Numerical experiments in boundary-layer stability. *Proc. R. Soc. Lond.* A **329**, 373–389.